










Cite this: *Nanoscale*, 2024, **16**, 4229

## Magnetic aerogels from FePt and CoPt<sub>3</sub> directly from organic solution†

L. Schoske, <sup>a,b,e,f</sup> F. Lübke-  
mann-Warwas, <sup>a,b</sup> I. Morales, <sup>a,b</sup> C. Wesemann, <sup>a</sup>  
J. G. Eckert, <sup>a,c</sup> R. T. Graf <sup>a,d</sup> and N. C. Bigall <sup>\*a,b,c,d,e,f</sup>

Here the synthesis of magnetic aerogels from iron platinum and cobalt platinum nanoparticles is presented. The use of hydrazine monohydrate as destabilizing agent triggers the gelation directly from organic solution, and therefore a phase transfer to aqueous media prior to the gelation is not necessary. The aerogels were characterized through Transmission Electron Microscopy, Scanning Electron Microscopy, Powder X-Ray Diffraction Analysis and Argon Physisorption measurements to prove the formation of a porous network and define their compositions. Additionally, magnetization measurements in terms of hysteresis cycles at 5 K and 300 K (M–H-curves) as well as zero field cooled-field cooled measurements (ZFC-FC measurements) of the dried colloids and the respective xero- and aerogels were performed, in order to analyze the influence of the gelation process and the network structure on the magnetic properties.

Received 20th November 2023,

Accepted 3rd February 2024

DOI: 10.1039/d3nr05892a

rsc.li/nanoscale

### Introduction

Magnetic nanoparticles have applications in various different fields such as catalysis, data storage, hyperthermia or drug delivery.<sup>1–4</sup> In particular, superparamagnetic nanoparticles have attracted a lot of attention due to their unique properties. Because of their small size these particles are single domain and the magnetic moments are randomly oriented due to thermal fluctuations; their net magnetization is zero in the absence of an applied magnetic field, which avoids their aggregation. In addition, superparamagnetic nanoparticles dissipate energy in the form of heat when they are subjected to alternating magnetic fields, which makes them especially interesting for biomedical applications such as magnetic hyperthermia.<sup>4–8</sup> There are also first reports on implementing magnetite nano-

particles to improve the mechanical stability of conductive concrete.<sup>9</sup>

Various magnetic alloys from transition metal alloys such as CoPt<sub>3</sub>, FePt, FePd, CoPd and FeCo to metal phosphides, ferrites and rare earth metal alloys such as SmCo<sub>5</sub>, Nd<sub>2</sub>Fe<sub>14</sub>B, Sm<sub>2</sub>Fe<sub>17</sub>N<sub>3</sub>, NdFeB<sup>10</sup> or (Nd, Ce)-Fe-B<sup>11</sup> are of great interest for various applications, because of high magnetic anisotropy, large coercivity and enhanced magnetic susceptibility.<sup>4</sup> Additionally, also magnetic semiconductors and half-metallic materials such as CrSI<sup>12</sup> have been investigated recently.

FePt shows two different phases, namely, the ordered fct and the disordered fcc-phase are known. While the ordered fct-phase shows ferromagnetic behavior with high magnetic saturation and a high magnetic anisotropy<sup>13</sup> the disordered fcc-phase shows a low magnetic saturation as well as a low magnetic anisotropy resulting in superparamagnetic behavior at room temperature.<sup>14</sup> As-prepared nanoparticles (NPs) exhibit the disordered fcc-phase. To convert the NPs from the disordered to the ordered-phase thermal annealing is necessary.<sup>15</sup> Cobalt platinum alloys are chemically stable<sup>16</sup> and epitaxial films of these alloys show a strong perpendicular magnetic anisotropy, which makes them interesting as magneto-optical recording media.<sup>17</sup> Similar to iron platinum nanoparticles, cobalt platinum nanoparticles show a disordered fcc structure after the synthesis as well as no hysteresis in the M–H-curve at 300 K.<sup>18</sup> In addition to that, the magnetic properties of nanoparticles are also highly dependent on their shape. The shape anisotropy has an influence on the coercivity and the blocking temperature, as it contributes to the effective anisotropy constant.<sup>4,19</sup> Up to now, mostly not connected mag-

<sup>a</sup>Institute of Physical Chemistry and Electrochemistry, Leibniz University Hannover, Callinstr. 3a, 30167 Hannover, Germany.

E-mail: nadja-carola.bigall@uni-hamburg.de

<sup>b</sup>Cluster of Excellence PhoenixD (Photonics, Optics and Engineering- Innovation Across Disciplines), Leibniz University Hannover, 30167 Hannover, Germany

<sup>c</sup>School of Additive Manufacturing, Ministry for Science and Culture of Lower Saxony, Hannover, Germany

<sup>d</sup>Laboratory of Nano and Quantum Engineering, Leibniz University Hannover, Schneiderberg 39, 30167 Hannover, Germany

<sup>e</sup>Institute of Physical Chemistry, University of Hamburg, Grindelallee 117, 20146 Hamburg, Germany

<sup>f</sup>The Hamburg Centre for Ultrafast Imaging, Hamburg, Germany

† Electronic supplementary information (ESI) available. See DOI: <https://doi.org/10.1039/d3nr05892a>



netic nanoparticles are used for various applications.<sup>1–8</sup> Instead, the combination of the high specific surface area, high porosity and low density<sup>20–22</sup> of porous structures, such as aerogels, with the magnetic properties of the colloidal nanoparticles would lead to materials with interesting properties that might be applicable for drug delivery or filtering systems.

An aerogel is considered as a porous network structure filled with air. Through controlled destabilization of the colloidal solution, the lyogel is formed. The pores of lyogels are filled with solvent, which has to be removed while drying without a collapse of the gel structure. Therefore, supercritical drying with CO<sub>2</sub> is performed to obtain aerogels out of lyogels. If lyogels are dried under ambient conditions, the capillary forces while drying lead to a collapse of the gel structure and therefore a compact structure (xerogels) is obtained.<sup>23,24</sup>

For noble metal<sup>25</sup> and metal chalcogenide nanoparticles,<sup>26</sup> a lot of different techniques to induce the self-assembly into networks were demonstrated<sup>23,27,28</sup> and the aerogel fabrication of semiconducting<sup>26–29</sup> and plasmonic<sup>23,25,30</sup> nanoparticles has been extensively investigated. Instead, the research into magnetic aerogels is still scarce and only some reports describe the formation of magnetic aerogels.<sup>31–35</sup> Anastasova *et al.*<sup>33,35</sup> as well as Ganonyan *et al.*<sup>34</sup> describe the synthesis of magnetite aerogels with the use of propylene oxide, following a sol-gel approach. In addition to that, Altenschmidt *et al.*<sup>36</sup> described the aerogelation of polymer-coated iron oxide nanoparticles through addition of calcium cations. While Berestok *et al.*<sup>31</sup> and Hettiarachchi *et al.*<sup>32</sup> already describe the formation of self-supported aerogels out of maghemite or Fe<sub>1.3</sub>Ni<sub>0.7</sub>P nanoparticles. In self-supported aerogels the particles are in direct contact with each other and the backbone only consists of nanoparticles as buildings blocks. Self-supported aerogels exhibit a large surface area and porous structures. Therefore, efficient mass transport and easy access to catalytic active sites are provided. The large surface area consisting only out of the catalytically active species leads to an improved catalytic activity of the material.<sup>22,37</sup> Nevertheless, more variety in magnetic aerogels is still needed, as well as a thorough magnetic characterization of the nanoparticles when they are part of a gel network.

For most gelation techniques, a phase transfer of the nanoparticles from organic to aqueous solution or a polar medium is necessary. The phase transfer is a time-consuming step and has to be adjusted for each type of nanoparticle separately. In addition to that, the ligand exchange, which is in most cases necessary to induce this phase transfer, might affect the surface of the nanoparticles and lead to undesirable property changes prior to gelation *e.g.* decrease of the quantum yield in case of semiconducting nanoparticle gels,<sup>38</sup> or spin canting and lower saturation magnetization for magnetic nanoparticles due to defects.<sup>39</sup> In the present work, a method described by Naskar *et al.*<sup>23</sup> was used to induce the assembly of platinum nanoparticles directly out of organic solution through hydrazine monohydrate as destabilizing agent. Hydrazine was discussed to bind to the platinum on the nanoparticle surface and leads to an oxidation and detachment of

the ligands.<sup>23</sup> In this work, we present the formation of porous aerogels out of iron platinum and cobalt platinum nanoparticles directly out of organic solution. The aerogels are characterized by scanning and transmission electron microscopy to prove the formation of a porous network out of interconnected nanoparticles. Measurements on a Super Conducting Quantum Interference Device (SQUID) were performed to investigate the influence of the gelation procedure and the network structure on the magnetic properties. It was found that for both discussed FePt-NPs (quasi-cubic and quasi-spherical particles) a change from paramagnetic to superparamagnetic behavior occurs after gelation. Instead, the superparamagnetism observed for CoPt<sub>3</sub>-NPs is preserved through gelation.

## Experimental

### Reagents

Platinum(II) acetylacetonate (Pt(acac)<sub>2</sub>, 98% ABCR, stored in glovebox), iron(0) pentacarbonyl (Fe(CO)<sub>5</sub>, 99.99% Sigma Aldrich, stored in fridge inside glovebox), hydrazine monohydrate (N<sub>2</sub>H<sub>4</sub>·H<sub>2</sub>O, 98% Sigma Aldrich), 1-octadecene (ODE, 90% Sigma Aldrich), oleic acid (90% Sigma Aldrich, stored in fridge), oleylamine (90% Sigma Aldrich), benzyl ether (98% Sigma Aldrich), 1,2-hexadecanediol (98% Sigma Aldrich), 1-adamantanecarboxylic acid (99% Sigma Aldrich), diphenyl ether (99% Acros), 1,2-dichlorobenzene (99% Sigma Aldrich, stored in Glovebox), hexadecylamine (HDA, ≥94% Merck), cobalt carbonyl (Co<sub>2</sub>(CO)<sub>8</sub>, ≥90% moistened with 1–10% *n*-hexane Sigma Aldrich, stored in fridge inside glovebox), isopropanol (≥99.8% Sigma Aldrich), *n*-hexane (≥99% Honeywell), acetone (≥99.5% Sigma Aldrich), ethanol (≥99.9% Sigma Aldrich), toluene (≥99.7% Sigma Aldrich), dried acetone (dried over molecular sieves 3 Å, distilled and stored in glovebox), hydrochloric acid (≥37% Sigma Aldrich), nitric acid (trace ≥99.999% Sigma Aldrich), liquid CO<sub>2</sub> (Linde 30 kg with riser tube). These chemicals were used without further purification.

### Synthesis FePt nanoparticles (FePt-NP)

Quasi spherical FePt-NPs with an average size of 5 nm were synthesized following a procedure from Schladt *et al.*<sup>13</sup> 0.1967 g platinum(II)-acetylacetonate, 10 mL benzyl ether and 5 mL ODE were degassed and stirred under vacuum for 1 h at 70 °C. Afterwards the flask was flushed with argon, and the temperature was increased to 120 °C. 264 μL Fe(CO)<sub>5</sub> and 1.6 mL oleic acid were injected under fast stirring. After 5 minutes, 1.6 mL oleylamine were injected. The mixture was heated up to 205 °C and kept for 1 h at this temperature. After that, the mixture was cooled down to room temperature, and subsequently 20 mL ethanol were added. The mixture was centrifuged for 10 min at 10 752 relative centrifugal force (RCF). The nanoparticles were redispersed in 5 mL *n*-hexane and 20 mL ethanol were added to continue the cleaning process. After centrifugation for additional 10 min at 10 752 RCF, the



nanoparticles were redispersed in 2 mL *n*-hexane. To stabilize the nanoparticles 25  $\mu$ L oleic acid and 25  $\mu$ L oleylamine were added. The nanoparticles were stored under ambient conditions in a glass vial.

### Synthesis CoPt<sub>3</sub> nanoparticles (CoPt<sub>3</sub>-NP)

Quasi spherical CoPt<sub>3</sub>-NPs with an average size of 7 nm were synthesized following a procedure by Shevchenko *et al.*<sup>18</sup> Briefly, 0.033 g Pt(acac)<sub>2</sub>, 0.13 g 1,2-hexadecanediol, 0.25 g 1-adamantanecarboxylic acid, 4.95 mL HDA and 2 mL diphenyl ether were degassed under stirring for 30 min at 65 °C. Afterwards the flask was flushed with argon and the mixture was heated up to 205 °C. After reaching the desired temperature, a solution of 0.014 g Co<sub>2</sub>(CO)<sub>8</sub> in 700  $\mu$ L of 1,2-dichlorobenzene, was injected and the mixture was kept at 205 °C for 1 h. The mixture was then heated up to 290 °C for 1.5 h. After the mixture was cooled down to 50 °C, 5 mL toluene as well as 20 mL isopropanol were added and the mixture was centrifuged for 10 min at 10 752 RCF. The nanoparticles were redispersed in 5 mL toluene, 20 mL isopropanol were added and the centrifugation was performed again for 10 min at 10 752 RCF. At the end the nanoparticles were redispersed in 2 mL of toluene and stored in a glass vial under ambient conditions.

### Synthesis FePt nanocubes (c-FePt-NP)

FePt nanocubes were synthesized following a procedure from Chou *et al.*<sup>40</sup> 0.047 g Pt(acac)<sub>2</sub>, 0.525 g 1,2-hexadecanediol and 2 mL oleic acid were degassed for 1 h at 70 °C under vacuum. After flushing the flask with argon the mixture was heated to 120 °C and 33  $\mu$ L Fe(CO)<sub>5</sub> were injected. The temperature was raised to 240 °C and kept for 1 h. After cooling down to room temperature 20 mL ethanol was added and the mixture was centrifuged for 10 min at 10 752 RCF. The nanoparticles were redispersed in 5 mL *n*-hexane and 20 mL ethanol were added. After centrifugation for 10 min at 10 752 RCF the nanoparticles were redispersed in 2 mL *n*-hexane and stored under ambient conditions in a glass vial.

### Synthesis of nanoparticle aerogels

In all three cases a nanoparticle solution containing 12 mg of platinum was centrifuged for 3 min at 10 752 RCF. The platinum concentration was determined by Inductively Coupled Plasma Optical Emission Spectroscopy measurements (ICP-OES). Afterwards the nanoparticles were redispersed in 400  $\mu$ L of *n*-hexane (FePt) or toluene (CoPt<sub>3</sub>). The gelation experiments were performed in 2 mL Eppendorf tubes. In case of FePt-NPs and c-FePt-NPs 30  $\mu$ L of hydrazine monohydrate were added to the nanoparticle solution, while for CoPt<sub>3</sub>-NPs 320  $\mu$ L hydrazine monohydrate were added. The mixture was shaken for a few seconds and stored free from vibrations for 2.5 h (FePt) or 4 h (CoPt<sub>3</sub>). Right after shaking a phase separation could be observed. A small clear phase can be seen on top of a black phase containing the nanoparticles. To stop the gelation the vials were carefully filled with the previous used solvent. Afterwards the solvent was replaced 6 times in intervals of 30 min with new solvent. Therefore about 1 mL of

solvent was removed by use of a plastic pipette and replaced with 1 mL of fresh toluene (CoPt<sub>3</sub>-NPs) or *n*-hexane (FePt-NPs/c-FePt-NPs). Afterwards the gel was stored for three days free from vibrations. The subsequent solvent exchange was performed over 2 days by gradually exchanging the solvent through ethanol (FePt) or acetone (CoPt<sub>3</sub>). For this purpose, 0.5 mL of solvent were replaced through 0.5 mL of acetone (CoPt<sub>3</sub>) or ethanol (FePt) with help of a plastic pipette. This procedure was repeated 5 times per day. Afterwards 1 mL of solvent above the gels were replaced five times a day for 5 days with 1 mL of fresh ethanol (FePt) or acetone (CoPt<sub>3</sub>). Finally, 1 mL of solvent was replaced by 1 mL of dry acetone (stored inside a glovebox) with the help of a plastic pipette. This procedure was repeated 5 times a day for 3 days to remove any remaining water or other solvent to prevent a collapse of the gel structure during supercritical drying. The supercritical drying was performed in a E3100 from Quorum technologies. The acetogels were placed into anhydrous acetone inside the autoclave. Inside, the acetone was replaced with liquid CO<sub>2</sub> and stayed in the dryer over night to ensure the diffusion of CO<sub>2</sub> into the pores. The dryer was then flushed for 5 minutes before heating up to 32 °C, so a pressure of 76 bar was reached. After CO<sub>2</sub> reached the supercritical state it was carefully released from the dryer as a gas.

### Scanning electron microscopy

The measurements were performed using a JOEL JSM-6700F with an acceleration voltage of 2 kV. For the measurement a small amount of the aerogel was deposited on a sticky carbon film and placed on a brass holder.

### Transmission electron microscopy

A Tecnai G2 TEM from FEI with an acceleration voltage of 200 kV was used for the measurements. The nanoparticle solutions were centrifuged 3 times before the sample preparation. Afterwards the nanoparticles were redispersed and diluted. 10  $\mu$ L of the redispersed and diluted nanoparticles were drop casted onto a carbon coated copper TEM-grid (300 mesh) from Quantifoil. In case of the acetogels a small amount of the gel was removed from the vial and sonicated for a few seconds. Afterwards the small fragments of the sonicated gel were drop casted onto the TEM-grid and dried under ambient conditions.

### Powder X-Ray diffraction analysis (XRD)

The measurements were performed with a Bruker D8 Advance. The nanoparticle solution was drop casted onto a single crystalline silicon wafer and dried under ambient conditions. The measurements were performed at room temperature with 40 kV and 30 mA of Cu K $\alpha$  radiation.

### IR measurements

The measurements were performed with a Cary 630 FTIR from Agilent Technologies. Oleylamine and oleic acid were mixed with hydrazine in a glass vial and a drop of this mixture was casted onto the device sample holder. In case of the ligands



present on the CoPt<sub>3</sub>-NPs surface, hexadecylamine and 1-Adamantanecarboxylic acid were mixed with hydrazine and the mixture was placed onto the sample holder.

### Inductively coupled plasma optical emission spectroscopy (ICP-OES)

The platinum, iron and cobalt concentrations were determined through Inductively Coupled Plasma Optical Emission Spectroscopy (ICP-OES) measurements with a 5110 ICP-OES from Agilent Technologies using argon as conductive gas for the plasma. 20  $\mu\text{L}$  of sample were decomposed overnight in 0.5 mL of aqua regia. A calibration curve was obtained by using Pt, Fe and Co standards for AAS to prepare 6 standards with concentrations between 0 and 7.5  $\text{mg L}^{-1}$  for Fe and Pt, and concentrations between 0 and 2.5  $\text{mg L}^{-1}$  for Co.

### Argon physisorption measurements

A Quantachrome Nova 3200e at 77 K was used for the physisorption measurements. The samples with masses between 2 and 6 mg were degassed for 30 h at room temperature. To estimate the specific surface area the Brunnauer–Emmett–Teller (BET)<sup>41</sup> equation was used.

### Magnetic measurements

Magnetic measurements were performed on a Quantum Design MPMS3 SQUID magnetometer on the dried nanoparticles, the regarding aero- and xerogels. The zero-field-cooled (ZFC) and field-cooled-measurements (FC) were performed with an applied 100 Oe DC field from 5 K to 300 K. The M–H-curve was measured at 5 K and 300 K from  $-70$  kOe to  $+70$  kOe in DC mode. All samples were measured in VSM Powder Sample Holders from Quantum Design. For all nanoparticle samples, the particle solution was casted dropwise in the sample holder and dried under ambient conditions. For preparation of xerogel samples small pieces of the acetogel were transferred by use of a pipette to the sample holder and dried under ambient conditions. Aerogel samples were prepared by placing small pieces of the aerogel into the sample holder.

## Results and discussion

Magnetic FePt and CoPt<sub>3</sub> nanoparticles were synthesized following the procedures from Schladt *et al.*,<sup>13</sup> Chou *et al.*,<sup>40</sup> and Shevchenko *et al.*,<sup>18</sup> respectively. To prove the formation of the desired particle shape and phase, XRD and TEM measurements were performed (Fig. 1A–C). All nanoparticles show a narrow size distribution with average sizes of 5  $\text{nm} \pm 0.8$  nm for FePt quasi-cubic and quasi spherical NPs and 7  $\text{nm} \pm 0.9$  nm for the quasi spherical CoPt<sub>3</sub>-NPs. From the XRD patterns it can be seen that all three nanoparticles match well with the reflexes of their corresponding unordered fcc-phase, which was expected as no thermal annealing was performed (Fig. 1D–F).

In order to find the best gelation parameters, different gelation experiments were performed. In all experiments, hydrazine was used to destabilize the solution. At first, different gelation times with a fixed amount of hydrazine solutions were used. The gelation times with the most voluminous gels were obtained after 2.5 h for iron platinum and 4 h for cobalt platinum (Fig. S1†). Experiments with varying amounts of hydrazine volumes were performed as well. The most voluminous gels with least shrinkage were observed after the addition of 30  $\mu\text{L}$  hydrazine for FePt and 320  $\mu\text{L}$  for CoPt<sub>3</sub> (Fig. S2 and S3†). To prove the successful formation of networks out of connected nanoparticles, TEM measurements as well as SEM measurements were performed (Fig. 2). The TEM images of the lyogels show a network structure in the lower magnification pictures (Fig. 2A–C) and a connection mostly through the nanoparticle surface in the higher resolution images (Fig. 2D–F). By comparison of the TEM pictures before and after the gelation it can be seen that no significant change in shape or size occurs during the gelation process. The nanoparticles retain their initial size and no melting together was observed. The SEM images (Fig. 2G–I) were taken after supercritical drying and therefore show the resulting aerogels. All samples show a porous structure, which indicates that both supercritical drying and gelation were successful. A similar structure for quasi spherical CoPt<sub>3</sub>-NPs and quasi spherical FePt-NPs were observed, while the structure for quasi cubic FePt-NPs appears to be slightly different. The quasi cubic sample appears to consist out of connected, porous small balls, while the quasi spherical samples show larger and less defined compartments. As this behavior is observed for both quasi-spherical samples out of different materials and different ligands, this behavior may be attributed to the particle shape. An influence of the facets cannot be excluded. As it can be seen in Fig. 2D–F the quasi-cubic sample is mainly connected through the edges and corners of the particles and shows a smaller contact area with neighboring particles in comparison to the quasi-spherical samples. The particle shape and the different type of connection during gelation can influence the structure of the aerogel<sup>24</sup> and may lead to the here observed structural differences. In general, a more compact structure compared to Naskar *et al.*<sup>23</sup> was obtained.

As mentioned above, the gelation technique that Naskar *et al.*<sup>23</sup> used to gel pure platinum nanoparticles was applied for the gelation experiments reported here. It was suggested by Naskar *et al.*<sup>23</sup> that the hydrazine binds onto the nanoparticle surface which results in oxidation and detachment of the previous ligands. The hydrazine then decomposes on the catalytically active surface of the platinum nanoparticles into hydrogen and nitrogen. It is suggested that hydrogen stays adsorbed onto the nanoparticle surface while nitrogen leaves the vial. This can be seen by small bubbles leaving the vial shortly after addition of hydrazine, which was also observed for all of the here described gelation experiments. The oxidation and detachment of the previous long chained organic ligands leads to a decrease of the steric repulsion. This causes a controlled destabilization of the platinum particles in the organic media,





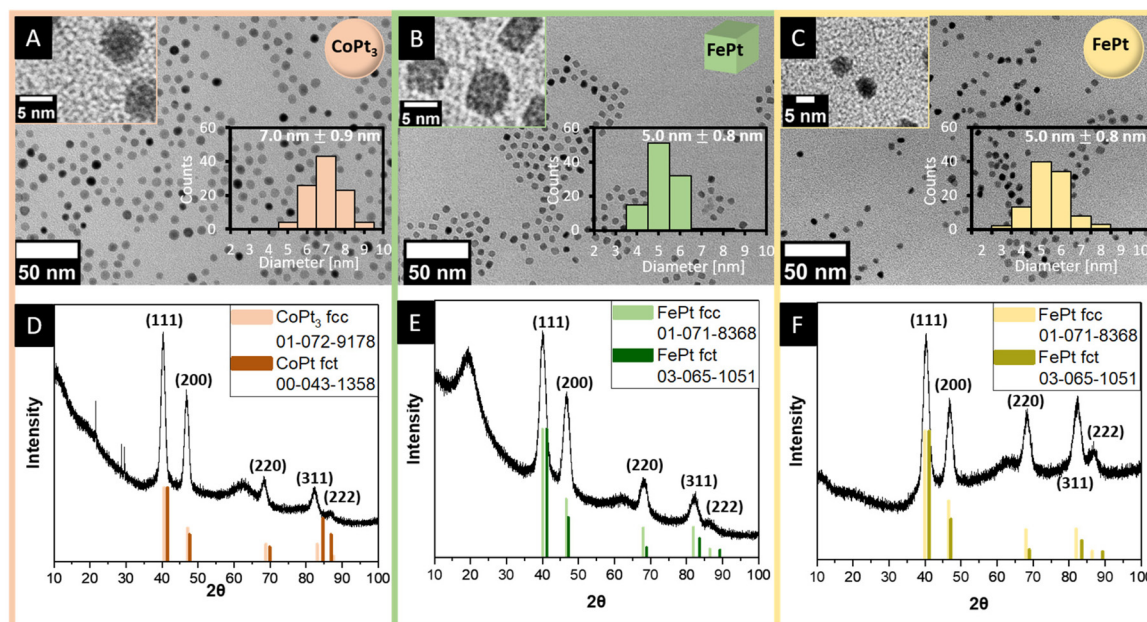


**Fig. 1** TEM images of (A) as synthesized quasi spherical  $\text{CoPt}_3$ -NPs, (B) FePt quasi-cubic NPs, (C) quasi spherical FePt NPs with the regarding size distributions and (D–F) XRD patterns.

a decreased distance between the individual particles and finally results in the formation of Pt–Pt metal bonds, which connect the individual particles to a porous network, the so called lyogel. Through solvent exchange to acetone and supercritical drying afterwards the lyogel is transformed into an aerogel. The gelation mechanism was described for oleylamine and oleic acid as ligands, which are present on the surface of the synthesized FePt-NPs. Therefore, a similar mechanism to the one proposed for pure platinum nanoparticles was expected. To proof this assumption, IR measurements were performed. The resulting IR spectra show no difference to the spectra observed by Naskar *et al.*<sup>23</sup> indicating that the mechanisms are similar for platinum and iron platinum (Fig. S4†). The carboxylic group of oleic acid binds onto the iron atoms on the surface of the iron platinum nanoparticles and forms an iron carboxylate, while oleylamine is coordinated onto the platinum atoms.<sup>42</sup> On the other hand, for the  $\text{CoPt}_3$ -NPs, a similar behavior is observed even with different ligands on the surface (Fig. S4†). The carboxylic acid (1-adamantanecarboxylic acid) binds onto the cobalt atoms while the amine (hexadecylamine) binds to the platinum atoms.<sup>18,42,43</sup> Schematic drawings of the ligands as well as the proposed gelation mechanisms are shown for both nanoparticle composition in Fig. 3. For both ligand mixtures, the signals from the amine can still be found, while the characteristic signal around  $1700\text{ cm}^{-1}$  from the carboxylic acid is not recognizable anymore. Instead, a signal around  $1500\text{ cm}^{-1}$  appears which is attributed to the O=C–N–H group and proves the formation of a hydrazinium complex.<sup>23</sup> This indicates that the hydrazine only reacts with the carboxylic acid and not with the amine. The spectra for both ligand mixtures are similar to each other suggesting a similar gelation mechanism for both nanoparticle compositions.

To evaluate the porosity and specific surface area of the aerogels, argon physisorption measurements were performed. The resulting isotherms as well as the regarding BET surfaces for all three aerogels are shown in Fig. 4. The FePt aerogels show a specific inner BET surface of  $9758\text{ m}^2\text{ mol}^{-1}$  ( $39\text{ m}^2\text{ g}^{-1}$ ) for quasi-cubic and  $9417\text{ m}^2\text{ mol}^{-1}$  ( $38\text{ m}^2\text{ g}^{-1}$ ) for spherical NPs, while the aerogel from  $\text{CoPt}_3$ -NPs shows a BET-surface of  $26566\text{ m}^2\text{ mol}^{-1}$  ( $41\text{ m}^2\text{ g}^{-1}$ ). In comparison to the maximum surface area for each sample, estimated for spherical and cubic nanoparticles from a geometric approximation with the corresponding sizes obtained *via* TEM, 48% in case of c-FePt-NPs, 46% in case of FePt-NPs and 85% of surface in case of  $\text{CoPt}_3$ -NPs are still available after formation of the aerogel. It can be seen in Fig. 2D–F that the quasi-spherical samples show a larger contact area with neighboring particles in comparison to the quasi-cubic sample. The quasi-cubic particles are connected mainly through the edges and corners of the cubes with smaller contact areas with neighboring particles. This leads to more accessible surface area after gelation in case of the quasi-cubic sample, and therefore a larger BET-surface is observed. Naskar *et al.*<sup>23</sup> obtained BET surface areas of  $35\text{ m}^2\text{ g}^{-1}$  and  $33\text{ m}^2\text{ g}^{-1}$  for aerogels of Pt cubes and Pt dots out of colloidal solutions with the same Pt concentration and nanoparticles size range as it was used here. The BJH<sup>44</sup> cumulative pore volumes are  $0.119\text{ cm}^3\text{ g}^{-1}$  (FePt-NPs),  $0.117\text{ cm}^3\text{ g}^{-1}$  ( $\text{CoPt}_3$ -NPs) and  $0.182\text{ cm}^3\text{ g}^{-1}$  (c-FePt-NPs) and the porous structures consist mainly of micro- (>2 nm) and meso pores (2–50 nm). The BET surface areas and isotherms clearly indicate the formation of porous aerogels with a high specific surface area as well as successful supercritical drying.

To investigate the influence of the gelation process on the magnetic properties, hysteresis cycles at 300 K (Fig. 5) and 5 K



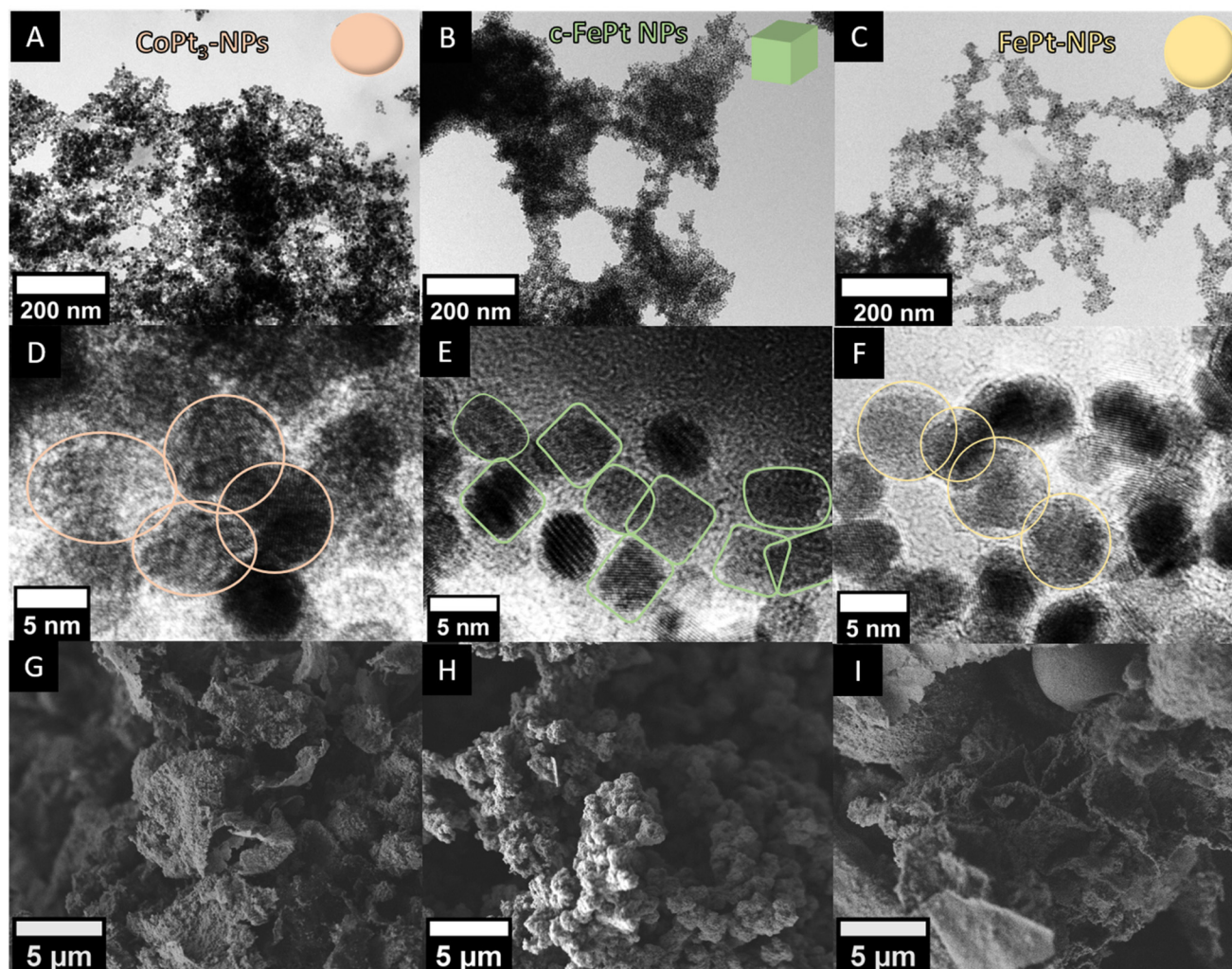


**Fig. 2** (A–C) TEM and (G–I) SEM images of porous structures formed through gelation and (D–F) HR-TEM images of the connected nanoparticles after the gelation for (A, D and G) quasi spherical  $\text{CoPt}_3$ -NPs, (B, E and H) FePt quasi-cubic and (C, F and I) quasi spherical NPs.

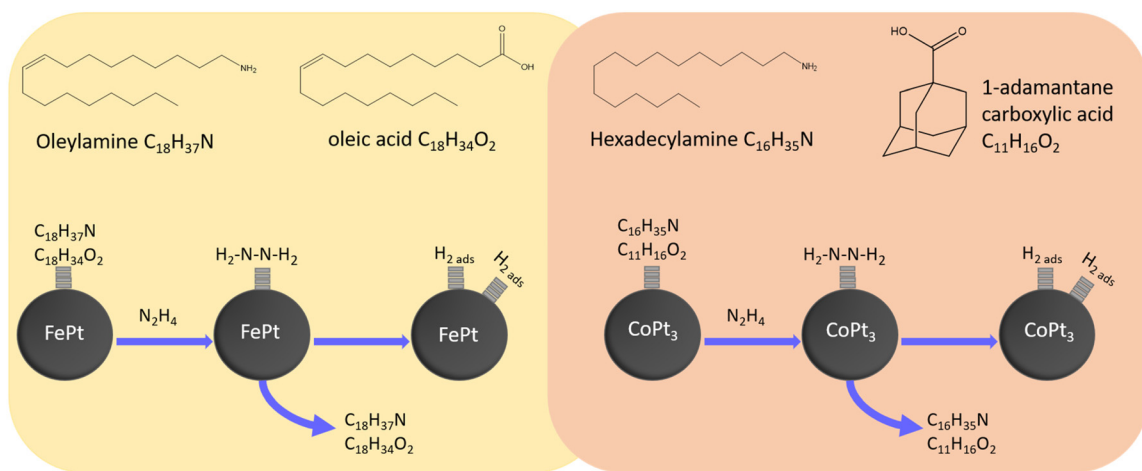


**Fig. 3** Scheme of ligands on the FePt and  $\text{CoPt}_3$  nanoparticle surface and a scheme of the suggested gelation mechanism for FePt and  $\text{CoPt}_3$  nanoparticles.





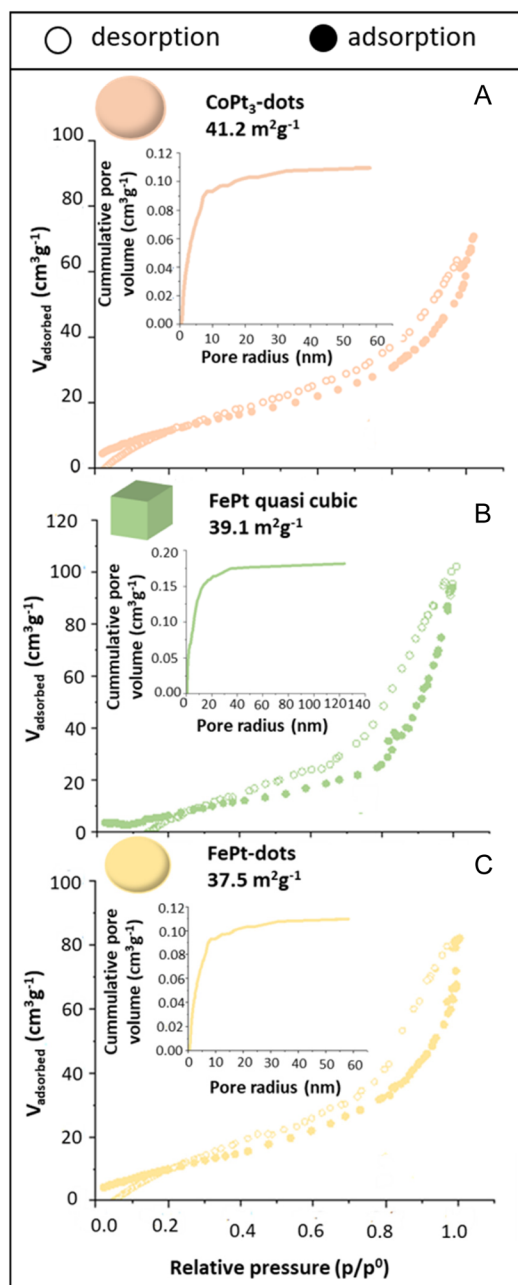


**Fig. 4** Argon physisorption measurements of (A) quasi spherical  $\text{CoPt}_3$ -NPs, (B) FePt quasi-cubic, (C) quasi spherical FePt-NPs and their specific BET-surfaces as well as the Barrett–Joyner–Halenda (BJH) cumulative pore volume distribution (insets).

(Fig. S5†) were performed before and after gelation. Measurements were acquired for the dried nanoparticle colloids, xero- and aerogels. In all cases, the magnetization is normalized to the total mass of the dried sample. For all samples, no annealing steps were performed on the particles and the particles show the disordered fcc-structure. This leads to superparamagnetic behavior at room temperature and in general much lower coercivity compared to annealed particles of the same species.<sup>45–49</sup> The hysteresis cycles of both nano-

particle compositions performed at 300 K are shown in Fig. 5. For all nanoparticle colloids the maximum magnetization at 300 K and 5 K is in agreement with the values found in literature for nanoparticles with similar size.<sup>4,45,50,51</sup> For all the samples, a decrease of the maximum magnetization after gelation compared to the nanoparticle colloids is observed at 5 K as well as for c-FePt-NP and  $\text{CoPt}_3$ -NP at 300 K (Fig. 5A, B and S5†), which indicates that the decrease is caused by the gelation process itself.<sup>4,31–33</sup>

The gelation process is induced by hydrazine addition in all cases. This leads to oxidation and removal of the ligands. During this process, etching of the surface might occur.<sup>32</sup> This leads to a decrease of the individual magnetic moment which in the case of c-FePt-NPs at 300 K is more pronounced than for  $\text{CoPt}_3$ -NPs at 300 K. While the decrease after the gelation is about 33% for  $\text{CoPt}_3$ -NPs, the decrease for c-FePt-NPs is around 57%. This can be explained by the smaller size of the FePt-NPs in comparison to the  $\text{CoPt}_3$ -NPs, which goes along with a higher specific surface (c-FePt-NPs:  $1.5 \times 10^{-16} \text{ m}^2$  per particle;  $\text{CoPt}_3$ -NPs:  $1.45 \times 10^{-16} \text{ m}^2$  per particle), and therefore etching has a higher impact on the c-FePt-NPs. In the case of  $\text{CoPt}_3$ -NPs, all measured hysteresis cycles at 300 K show superparamagnetic behavior. In contrast, the quasi spherical FePt-NPs and quasi-cubic nanoparticles show superparamagnetic behavior only after gelation. The curves for the xero- and aerogel for quasi-cubic FePt sample saturates at high fields. Instead, we still observe a slope at high fields in the case of spherical FePt-NPs. This might be due to the shape difference of both nanoparticles. In the case of both FePt nanoparticles, the hysteresis cycle at 300 K shows an almost linear behavior which is typically observed for paramagnetic materials.<sup>52</sup> Similar behavior for small fcc FePt nanoparticles is already known in literature.<sup>46,53,54</sup> One contribution to this behavior could be the presence of a nonmagnetic layer at the surface of the nanoparticles due to oxidation of the oleic acid.<sup>50,54–56</sup> The thickness of this layer is dependent on the chain length and  $\text{p}K_b$ -value of the ligand. With higher basicity the electron donation from the ligands to the d-band of Fe increases. Therefore, the thickness of the dead layer is increased and the magnetic saturation of the nanoparticles in comparison to the bulk material is further decreased.<sup>54,55</sup> In case of the 5 nm FePt nanoparticles, the thickness of the so-called dead layer was calculated to be around 1.64 nm. In addition to that, the as synthesized nanoparticles show a composition of  $\text{Fe}_{0.25}\text{Pt}_{0.75}$ , which was obtained from ICP-OES measurements. This phase has been reported to have a Curie temperature near to room temperature.<sup>57</sup> A combination of those two factors leads to the high paramagnetic contribution which can be observed for the M–H-curve of FePt nanoparticles at 300 K, leading to no saturation at high fields and an almost constant slope.

The ZFC-FC curves measured with a DC field of 100 Oe and shown in Fig. 5D–F, prove that all analyzed gels are in the superparamagnetic regime at 300 K. For the measurement of ZFC curves the sample was cooled down to 5 K without any field applied. Afterwards the sample was heated to 300 K and



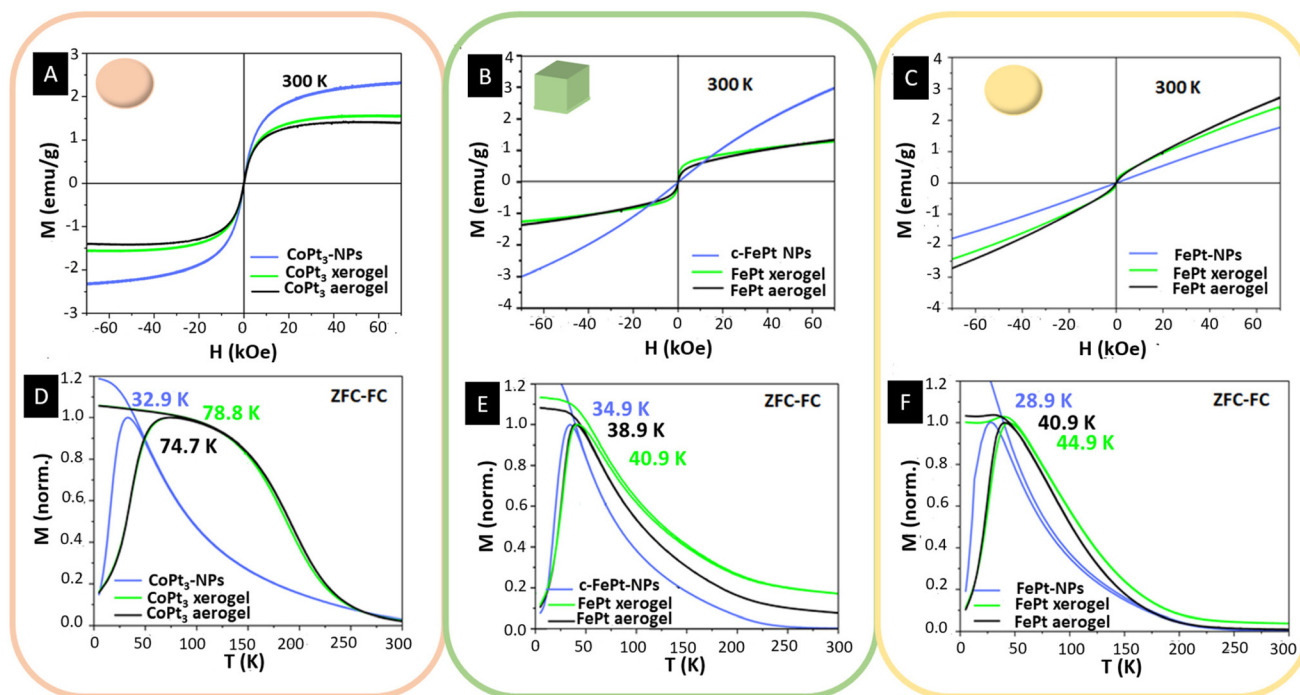


Fig. 5 Hysteresis cycles measured at 300 K and 7 T of the nanoparticles before (blue) and after gelation (green and black) for (A) quasi spherical CoPt<sub>3</sub>-NPs, (B) quasi cubic FePt-NPs (C) and quasi spherical FePt-NPs. ZFC-FC curves measured at 100 Oe and shift of the blocking temperature  $T_B$  through gelation from (D) quasi spherical CoPt<sub>3</sub>-NPs (E) quasi cubic FePt-NPs and (F) quasi spherical FePt-NPs.

during this step a magnetic field of 100 Oe was applied. To make sure that the measurements are comparable with each other the same method was used for all samples. The FePt nanoparticles show for both shapes a low magnetization at 300 K and only a small shift of the blocking temperature from 34.9 K (quasi-cubic) and 28.9 K (quasi spherical) before to 38.9 K and 40.9 K after gelation. The slightly higher blocking temperature in case of the quasi-cubic nanoparticles compared to the spherical ones with similar size is attributed to the higher volume of the quasi-cubic shaped nanoparticles ( $1.5 \times 10^{-16} \text{ m}^3$ ) compared to the quasi spherical nanoparticles ( $7.85 \times 10^{-17} \text{ m}^3$ ).<sup>58</sup> Both curves show a narrow peak, which indicates that all nanoparticles in the sample have a similar blocking temperature and therefore, a narrow size distribution which is in agreement with the TEM images (Fig. 2 and Fig. S1†). The TEM images show that the nanoparticles are in close contact after the gelation. The effective anisotropy  $K_{\text{eff}}$  increases while decreasing the distance between the nanoparticles due to the increased dipolar interactions, and therefore, the blocking temperature is increased.<sup>59</sup> Interestingly, the blocking temperature of the xerogels, in all cases, is higher than that of the respective aerogels, originating from the more compact structure and therefore from a reduced effective distance between the nanoparticles in the material.<sup>60</sup> Also in case of the CoPt<sub>3</sub> nanoparticles, a shift of the blocking temperature after gelation is observed. This can be attributed as well to a closer contact of the nanoparticles and therefore an increased  $K_{\text{eff}}$ . The shift of the blocking temperature to higher tempera-

tures through gelation is more pronounced for the CoPt<sub>3</sub> nanoparticles than for the FePt-NPs. The blocking temperature shifts from 32.9 K before to 74.7 K after the gelation. The blocking temperature depends on the volume of the nanoparticles and on the magnetic anisotropy. The nanoparticles retain their size during gelation, as can be seen from the HRTEM images (Fig. 2). Because of the larger nanoparticle size of CoPt<sub>3</sub>-NP, the percentage of surface atoms is decreased in comparison to the FePt-NPs. The influence of surface etching through the gelation process is decreased as well and therefore a higher percentage of atoms can interact with surrounding nanoparticles. In addition to that the CoPt<sub>3</sub> nanoparticles are in closer contact after the gelation (Fig. 2) than the FePt nanoparticles, leading to a stronger increase of  $K_{\text{eff}}$  and therefore a stronger shift of the blocking temperature.

## Conclusion

In conclusion, we not only proved that the gelation procedure by Naskar *et al.*<sup>23</sup> is also applicable for alloys containing platinum, but also reported, to our knowledge, the first synthesis of self-supported FePt and CoPt<sub>3</sub>- aerogels and investigated their magnetic properties in comparison to their xerogels and their nanoparticle building blocks. Additionally, the influence of the gelation procedure on the magnetic properties was investigated and we observed a strong influence on the magnetic properties of materials through the gelation process. In





all cases a decrease of the saturation magnetization was observed after the gelation. This is attributed to surface etching through oxidation and removal of the ligands and is more pronounced in case of the smaller FePt particles. In Addition to that, we also observed for both FePt samples measured at room temperature a change from almost paramagnetic behavior before the gelation to superparamagnetic behavior afterwards, because of their small particle size and closer particle contact in the gel network. We therefore showed the non-negligible influence of gelation procedures on the magnetic properties of materials. This knowledge is necessary to develop and tailor new materials suitable for various future applications combining their magnetic properties with the huge surface area of gels.

## Conflicts of interest

There are no conflicts to declare.

## Acknowledgements

This work is supported by the Cluster of Excellence CUI: Advanced Imaging of Matter' of the Deutsche Forschungsgemeinschaft (DFG)-EXC2056- project ID 390715994. The authors would like to thank the German Research Foundation (Deutsche Forschungsgemeinschaft, DFG) for funding under Germany's excellence strategy within the cluster of excellence PhoenixD (EXC2122, project ID 390833453). The authors are also thankful for financial support from the German Research Foundation (Deutsche Forschungsgemeinschaft, DFG, Projects BI 1708/4-3 and INST 187/782-1) R.T.G. thank the Hannover School of Nanotechnology (HSN) for funding. J. G. E. thanks the School of Additive Manufacturing for support. The authors thank the Laboratory of Nano- and Quantum Engineering (LNQE) for providing the TEM facilities, Prof. Armin Feldhoff for providing SEM facilities and access to the XRD device, as well as Kirsten Eiben for providing access to the ICP-OES. We acknowledge financial support from the Open Access Publication Fund of Universität Hamburg.

## References

- 1 A. K. Gupta and M. Gupta, *Biomaterials*, 2005, **26**, 3995–4021.
- 2 T. Hyeon, *Chem. Commun.*, 2003, 927–934.
- 3 M. Colombo, S. Carregal-Romero, M. F. Casula, L. Gutiérrez, M. P. Morales, I. B. Böhm, J. T. Heverhagen, D. Prospero and W. J. Parak, *Chem. Soc. Rev.*, 2012, **41**, 4306–4334.
- 4 A.-H. Lu, E. L. Salabas and F. Schüth, *Angew. Chem., Int. Ed.*, 2007, **46**, 1222–1244.
- 5 C. Berry and A. Curtis, *J. Phys. D: Appl. Phys.*, 2003, **36**(13), R198–R206.
- 6 A. K. Gupta and M. Gupta, *Biomaterials*, 2005, **26**, 3995–4021.
- 7 S. Mornet, S. Vasseur, F. Grasset and E. Duguet, *J. Mater. Chem.*, 2004, **14**(14), 2161.
- 8 H. Gavilán, S. Avugadda, T. Fernández-Cabada, N. Soni, M. Cassani, B. Mai, R. Chantrell and T. Pellegrino, *Chem. Soc. Rev.*, 2021, **50**(20), 11614–11667.
- 9 Z. Ren, H. Zheng, X. Zeng, X. Chen and X. Wang, *Buildings*, 2023, **13**, 1630.
- 10 Z. Ma, J. Mohapatra, K. Wie, P. Liu and S. Sun, *Chem. Rev.*, 2023, **123**(7), 3904–3943.
- 11 Q. Sun, M. Zhu, Q. Wang, C. Zhu, J. Yang and W. Li, *Acta Mater.*, 2023, **246**, 118703.
- 12 I. Muhammad, A. Ali, L. Zhou, W. Zhang and P. Wong, *J. Alloys Compd.*, 2022, **909**, 164797.
- 13 T. D. Schladt, T. Graf, O. Köhler, H. Bauer, M. Dietzsch, J. Mertins, R. Branscheid, U. Kolb and W. Tremel, *Chem. Mater.*, 2012, **24**(3), 525–535.
- 14 M. Ulmeanu, C. Antonaik, U. Wiedald, M. Farle, Z. Frait and S. Sun, *Phys. Rev. B: Condens. Matter Mater. Phys.*, 2004, **69**, 54417.
- 15 M. Chen, J. Kim, J. P. Liu, H. Fan and S. Sun, *J. Am. Chem. Soc.*, 2006, **128**, 7132–7133.
- 16 E. V. Shevchenko, D. V. Talapin, H. Schnablegger, A. Kornowski, Ö. Festin, P. Svedlindh, M. Maase and H. Weller, *J. Am. Chem. Soc.*, 2003, **125**, 9090–9101.
- 17 M. Maret, M. C. Cadeville, R. Poinot, A. Herr, E. Beaurepaire and C. Monier, *J. Magn. Magn. Mater.*, 1997, 45–52.
- 18 E. V. Shevchenko, D. V. Talapin, A. L. Rogach, A. Kornowski, M. Haase and H. Weller, *J. Am. Chem. Soc.*, 2002, **124**, 11480.
- 19 S. Oyarzún, A. Tamion, F. Tournus, V. Dupius and M. Hillenkamp, *Sci. Rep.*, 2015, **5**(1), 14749.
- 20 N. Hüsing and U. Schubert, *Angew. Chem., Int. Ed.*, 1998, **37**, 22–45.
- 21 C. Ziegler, A. Wolf, W. Liu, A. K. Herrmann, N. Gaponik and A. Eychmüller, Modern Inorganic Aerogels, *Angew. Chem., Int. Ed.*, 2017, **56**, 13200–13221.
- 22 B. Cai and A. Eychmüller, *Adv. Mater.*, 2019, **31**, 1804881.
- 23 S. Naskar, A. Freytag, J. Deutsch, N. Wendt, P. Behrens, A. Köckritz and N. C. Bigall, *Chem. Mater.*, 2017, **29**, 9208–9217.
- 24 P. Rusch, D. Zámbo and N. Bigall, *Acc. Chem. Res.*, 2020, **53**(10), 2414–2424.
- 25 H. Wang, Q. Fang, W. Gu, D. Du, Y. Lin and C. Zhu, *ACS Appl. Mater. Interfaces*, 2020, **12**, 52234–52250.
- 26 P. Rusch, D. Pluta, F. Lübke, D. Dorfs, D. Zámbo and N. C. Bigall, *ChemPhysChem*, 2022, **23**, e202100755.
- 27 D. Zámbo, A. Schlosser, P. Rusch, F. Lübke, J. Koch, H. Pfnür and N. C. Bigall, *Small*, 2020, **16**, 1906934.
- 28 J. L. Mohanan and S. L. Brock, *J. Non-Cryst. Solids*, 2004, 1–8.
- 29 S. Sánchez-Paradinas, D. Dorfs, S. Friebe, A. Freytag, A. Wolf and N. Bigall, *Adv. Mater.*, 2015, **27**(40), 6151–6151.
- 30 A. Hermann, W. Liu, N. Gaponik, N. Bigall and A. Eychmüller, *ECS Trans.*, 2003, **45**(20), 149–154.



- 31 T. Berestok, J. Chacón-Borrero, P. Guardia and A. Cabot, *Langmuir*, 2023, **39**(10), 3692–3698.
- 32 M. A. Hettiarachchi, T. Suá, A.-H. Ramzan, S. Pokhrel, B. Nadgorny and S. L. Brock, *J. Phys. Chem. C*, 2022, **126**(4), 2088–2097.
- 33 E. Anastasova, D. Puzyrev, V. Ivanovski and A. Drozdov, *J. Magn. Magn. Mater.*, 2020, **166619**, 503.
- 34 N. Ganonyan, J. He, A. Temkin, I. Felner, R. Gvishi and D. Avnir, *Appl. Mater. Today*, 2021, **100955**, 22.
- 35 E. Anastasova, V. Ivanovski, A. Fakhardo, A. Lepshkin, S. Omar, A. Drozdov and V. Vinogradov, *Soft Matter*, 2017, **13**(45), 8651–8660.
- 36 L. Altenschmidt, S. Sánchez-Paradinas, F. Lübke, D. Zámbo, A. Abdelmonem, H. Bradtmüller, A. Masood, I. Morales, P. de la Presa, A. Knebel, M. Garcia-Tunón, B. Pelaz, K. Hindricks, P. Behrens, W. Parak and N. Bigall, *ACS Appl. Nano Mater.*, 2021, **4**(7), 6678–6688.
- 37 L. Wei, A. Herrmann, N. Bigall, P. Rodriguez, D. Wen, M. Oezaslan, T. Schmidt, N. Gaponik and A. Eychmüller, *Acc. Chem. Res.*, 2015, **48**, 154–162.
- 38 D. Dorokhin, N. Tomczak, M. Han, D. Reinhoudt, A. Velders and G. Ancso, *ACS Nano*, 2009, **3**(3), 661–667.
- 39 W. Baaziz, B. P. Pichon, S. Fleutot, Y. Liu, C. Lefevre, J. M. Greneche, M. Toumi, T. Mhiri and S. Begin-Colin, *J. Phys. Chem. C*, 2014, **118**(7), 3795–3810.
- 40 S.-W. Chou, C.-L. Zhu, S. Neeleshwar, C.-L. Chen, Y.-Y. Chen and C.-C. Chen, *Chem. Mater.*, 2009, **21**(20), 4955–4961.
- 41 S. Brunauer, P. Emmett and E. Teller, *J. Am. Chem. Soc.*, 1938, **60**(2), 309–319.
- 42 S. Sun, *Adv. Mater.*, 2006, **18**, 393–403.
- 43 G. Krylova, N. M. Dimitijevic, D. V. Talapin, J. R. Guest, H. Borchert, A. Lobo, T. Rajh and E. V. Shevchenko, *J. Am. Chem. Soc.*, 2010, **132**, 9102–9110.
- 44 E. Barrett, L. Joyner and P. Halenda, *J. Am. Chem. Soc.*, 1951, **73**(1), 373–380.
- 45 H. L. Nguyen, L. E. M. Howard, G. W. Stinton, S. R. Giblin, B. K. Tanner, I. Terry, A. K. Hughes, I. M. Ross, A. Serres and J. S. O. Evans, *Chem. Mater.*, 2006, **18**(26), 6414–6424.
- 46 M. S. Seehra, V. Singh, P. Dutta, S. Neeleshwar, Y. Y. Chen, C. L. Chen, S. W. Chou and C. C. Chen, *J. Phys. D: Appl. Phys.*, 2010, **43**, 145002.
- 47 V. Nandwana, K. E. Elkins, N. Poudyal, G. S. Chaubey, K. Yano and J. P. Liu, *J. Phys. Chem. C*, 2007, **111**(11), 4185–4189.
- 48 X. Sun, Z. Jia, Y. Huang, J. Harrel, D. Nikles, K. Sun and L. Wang, *J. Appl. Phys.*, 2004, **95**, 6747–6749.
- 49 P. Karipoth and R. Joseyphus, *J. Supercond. Novel Magn.*, 2014, **27**, 2123–2130.
- 50 P. De la Presa, T. Rueda, A. Hernando, J. M. Ramallo-López, L. J. Giovanetti and F. G. Requejo, *J. Appl. Phys.*, 2008, **103**, 103909.
- 51 E. Shevchenko, D. Talapin, H. Schnablegger, A. Kornowski, Ö. Festin, P. Svedlindh, M. Haase and H. Weller, *J. Am. Chem. Soc.*, 2003, **125**(30), 9090–9101.
- 52 S. Singh, Kanika, G. Kedawat, J. H. Park, B. Ghorai, U. K. Ghorai, C. Upadhyay, B. A. Kaiparettu and B. K. Gupta, *J. Photochem. Photobiol.*, 2021, **8**, 100081.
- 53 V. Nandwana, K. E. Elkins, N. Poudyal, G. S. Chaubey, K. Yano and J. P. Liu, *J. Phys. Chem. C*, 2007, **111**(11), 4185–4189.
- 54 M. Delalande, P. R. Marcoux, P. Reiss and Y. Samson, *J. Mater. Chem.*, 2007, **17**, 1579–1588.
- 55 Y. Tanaka, S. Saita and S. Maenosono, *Appl. Phys. Lett.*, 2008, **92**, 093117.
- 56 X. W. Wu, C. Liu, L. Li, P. Jones, R. W. Chantrell and D. Weller, *J. Appl. Phys.*, 2004, **95**, 6810.
- 57 A. Kussmann and G. V. Rittberg, *Z. Metallkd.*, 1950, **41**, 470.
- 58 K. V. Chandekar and K. M. Kant, *Phys. B*, 2017, **520**, 152–163.
- 59 W. C. Nunes, L. M. Socolovsky, J. C. Denardin, F. Cebollada, A. L. Brandl and M. Knobel, *Phys. Rev. B: Condens. Matter Mater. Phys.*, 2005, **72**(21), 212413.
- 60 F. Fabris, K.-H. Tu, C. A. Ross and W. C. Nunes, *J. Appl. Phys.*, 2019, **126**, 173905.

